Research Square

Preprints are preliminary reports that have not undergone peer review.
They should not be considered conclusive, used to inform clinical practice,
or referenced by the media as validated information.

Unsupervised chemical-space organization enables identification of self-healing yet ultra-robust polyurethane elastomers

Zhigang Xue

zgxue@mail.hust.edu.cn

Huazhong University of Science and Technology https://orcid.org/0000-0003-2335-9537

Dian Liu

Huazhong University of Science and Technology

Zhen Shi

Huazhong University of Science and Technology

Junchen Meng

Huazhong University of Science and Technology

Xiaoyu Ji

National Key Laboratory of Electromagnetic Energy, Naval University of Engineering
https://orcid.org/0009-0004-1477-1815

Article

Keywords:

Posted Date: November 19th, 2026

DOI: https://doi.org/10.21203/rs.3.rs-11579608/v1

License: This work is licensed under a Creative Commons Attribution 4.0 International License.
Read Full License

Additional Declarations: There is **NO** Competing Interest.

Unsupervised chemical-space organization enables identification of self-healing yet ultra-robust polyurethane elastomers

Dian Liu[1,#], Zhen Shi[1,#], Junchen Meng[1], Xiaoyu Ji[2,*] & Zhigang Xue[1,*]

[1]Key Laboratory of Material Chemistry for Energy Conversion and Storage, Ministry of Education, Hubei Key Laboratory of Material Chemistry and Service Failure, School of Chemistry and Chemical Engineering, Huazhong University of Science and Technology, Wuhan 430074, China

[2]National Key Laboratory of Electromagnetic Energy, Naval University of Engineering, Wuhan, China.

[#]These authors contributed equally.

*Correspondence to Zhigang Xue (zgxue@mail.hust.edu.cn) and Xiaoyu Ji (xiaoyu.ji@nue.edu.cn)

Abstract

Although published polyurethane formulations contain detailed structural information, inconsistent measurement protocols limit their utility in data-driven materials discovery. We introduce an unsupervised chemical-space organization strategy that maps 296 literature formulations alongside millions of virtual combinations onto a shared 13-descriptor representation. Uniform manifold approximation and projection (UMAP) and hierarchical density-based spatial clustering of applications with noise (HDBSCAN) partition the space, while a geometry-based ranking anchored to literature formulations

with tensile strength >20 MPa and healing efficiency >0.90 generates the candidate queue. After screening for formulation plausibility, reagent availability, and synthetic accessibility, six candidates were selected for experimental comparison. The resulting formulation, PUUB (PC2000/HMDI/UPy/PBA), integrates ureidopyrimidinone quadruple hydrogen bonding with phenylboronic-acid-derived dynamic boroxine motifs. PUUB achieves a tensile strength of approximately 98 MPa at 788% elongation, a tensile work-to-fracture of 297 MJ m^{-3}, and 86.5% fracture-strength recovery after a four-fifths-width cut and 24 h at 80 °C in the presence of water. This workflow converts heterogeneous literature data into prioritized, experimentally validated candidates, providing a generalizable strategy for designing materials with complex, coupled properties.

Introduction

Polyurethanes are widely used in coatings, adhesives, flexible electronics, and mechanically compliant components because their segmented architectures can be readily tailored to achieve a broad spectrum of mechanical performance[1,2]. Combining load-bearing capacity with self-healing ability could extend service life after damage, yet the molecular interactions that strengthen a network can also restrict the chain mobility required for repair. Supramolecular and dynamically bonded polymers have demonstrated that these functions can coexist within a single network[3-6]. In segmented polyurethanes, hydrogen-bonding motifs, soft/hard segment matching, microphase-separated morphology, and dynamic crosslinking collectively govern mechanical reinforcement and molecular rearrangement[7-11]. Identifying compatible combinations across these coupled design variables remains a central challenge.

Soft segments, diisocyanates, and chain extenders can be combined to tune polarity,

flexibility, and reversible interactions, but the vast number of possible combinations makes systematic selection difficult. Existing examples range from vanillin-derived polyurethane[12] to waterborne polyurethane micelles, thiourethane-based elastomeric electrolytes, and phase-organized polyurea electrolytes[13-15], as well as quadruple-hydrogen-bonded, dual-network, and photonic materials[16-18]. While these studies highlight useful chemical motifs, formulations and measurement conditions vary widely. Tensile strength depends on specimen preparation and testing protocols, and reported healing efficiencies depend on damage geometry, temperature, time, and the specific property used to calculate recovery. Consequently, literature values do not constitute a consistent dataset for supervised property prediction.

Artificial intelligence provides tools for exploring large combinatorial spaces in chemical research[19,20]. Chemical-language representations and stoichiometry-based representation learning offer complementary routes to encoding materials information[21,22]. Machine-learning studies have examined biomass-based polyurethane adhesives, polyurethane elastomer properties, and ionic polymer electrolytes[23-25], and related work has designed mechanically robust self-healing epoxy resins[26]. In other material systems, active learning, unsupervised discovery, language representations, and clustering have supported candidate screening[27-31]. For polyurethane literature with heterogeneous measurements, unsupervised representations can organize formulations by structural and compositional similarity: chemically similar formulations cluster together, and regions containing high-performing literature anchors provide an empirical basis for prioritizing new combinations. Dimensionality reduction, density-based clustering, and geometry-based ranking make this prioritization explicit, after which candidate performance is assessed experimentally.

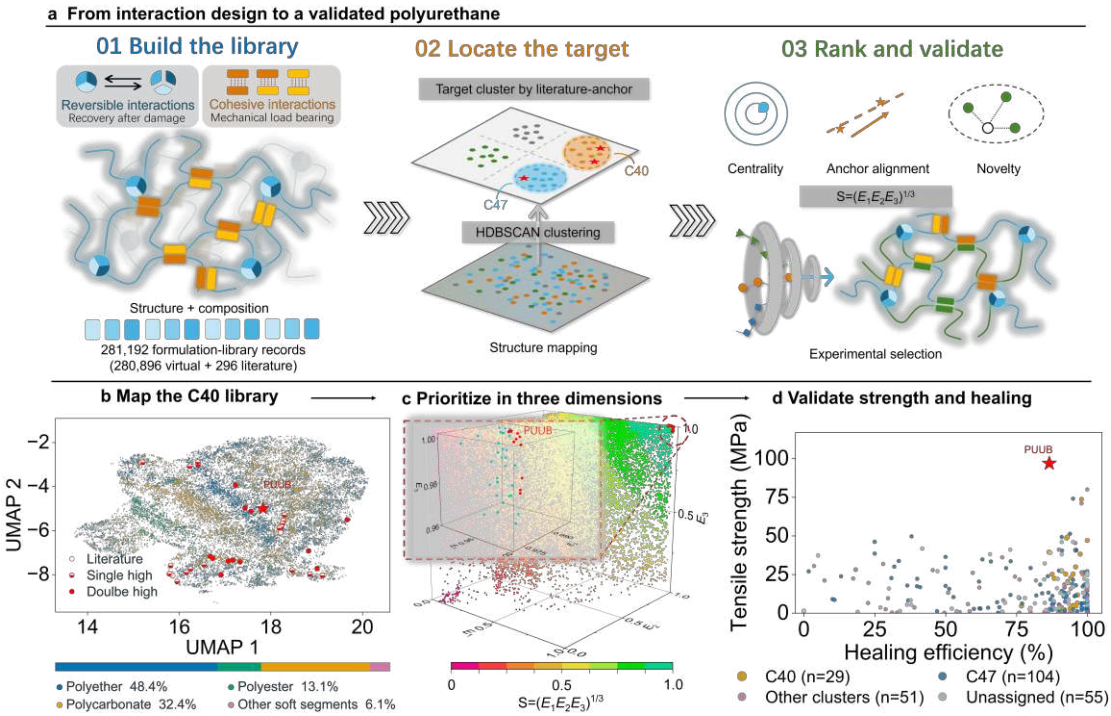


Fig. 1 | Workflow for organizing polyurethane formulations and selecting candidates for experimental validation. a Formulation representation and library construction, followed by chemical-space mapping, regional prioritization, candidate ranking, and experimental validation. **b** C40 chemical-space map of virtual formulations and literature anchors, colored by soft-segment family. **c** Geometric score space (E1-E3) for candidate ranking. **d** Reported tensile strength and healing efficiency for literature formulations with paired measurements and PUUB.

Here we present a workflow for organizing and prioritizing polyurethane formulations when literature measurements are heterogeneous. Literature formulations and virtual combinations share a common descriptor representation; high-performing literature formulations guide regional selection; and three geometric scores define the candidate queue. Screening for formulation plausibility, reagent availability, and synthetic accessibility narrows the queue to six candidates. Experimental comparison identified PUUB as the strongest of the six candidates before and after healing, experimentally validating the selection strategy. **Fig. 1** summarizes the route from formulation-library construction to literature-guided regional selection, geometric ranking, and experimental validation. Briefly, 296 literature formulations were combined with 280,896 virtual formulations and encoded using 13 structural and compositional

descriptors. UMAP and HDBSCAN partitioned the shared chemical space into 57 clusters, and geometric scores E1-E3 ranked virtual candidates within the two retained regions, C40 and C47. The candidate queue was filtered by formulation plausibility, reagent availability, and synthetic accessibility, yielding six formulations for synthesis and experimental comparison, from which the C40 rank-10 polycarbonate soft segment (PC2000)/aliphatic diisocyanate (HMDI)/quadruple hydrogen bonding (UPy)/phenylboronic acid (PBA) formulation (PUUB) was selected for detailed characterization. PUU (with UPy but no PBA) and PUB (with PBA but no UPy) were prepared as chemically simpler controls to isolate the contributions of the UPy-containing extender and the PBA-derived component. The lower row connects the C40 chemical-space map and E1-E3 ranking to the literature-performance context of the experimentally selected PUUB formulation.

Results

A literature-informed representation defines the formulation search space

To define the search space, we combined 296 literature formulations with a virtual library generated from 22 soft segments, eight diisocyanates, and 56 chain extenders. Treating chain-extender combinations as 1,596 unordered pairs yielded 280,896 virtual formulations (22 × 8 × 1,596). **Fig. 2**a summarizes the path from component inventory to descriptor construction and dimensionality reduction. Literature entries retained formulation identity and reported tensile or healing values where available, and virtual entries supplied chemically traceable combinations encoded in the same representation. **Fig. 2**b,c illustrates the completeness of literature formulation and performance fields alongside the sparse literature coverage of component-pair combinations. The resulting formulation library contains 281,192 records: 280,896 virtual formulations and 296 external literature formulations (Supplementary Fig. S1; Supplementary Tables S1 and

S2 (external Excel workbooks) and S3).

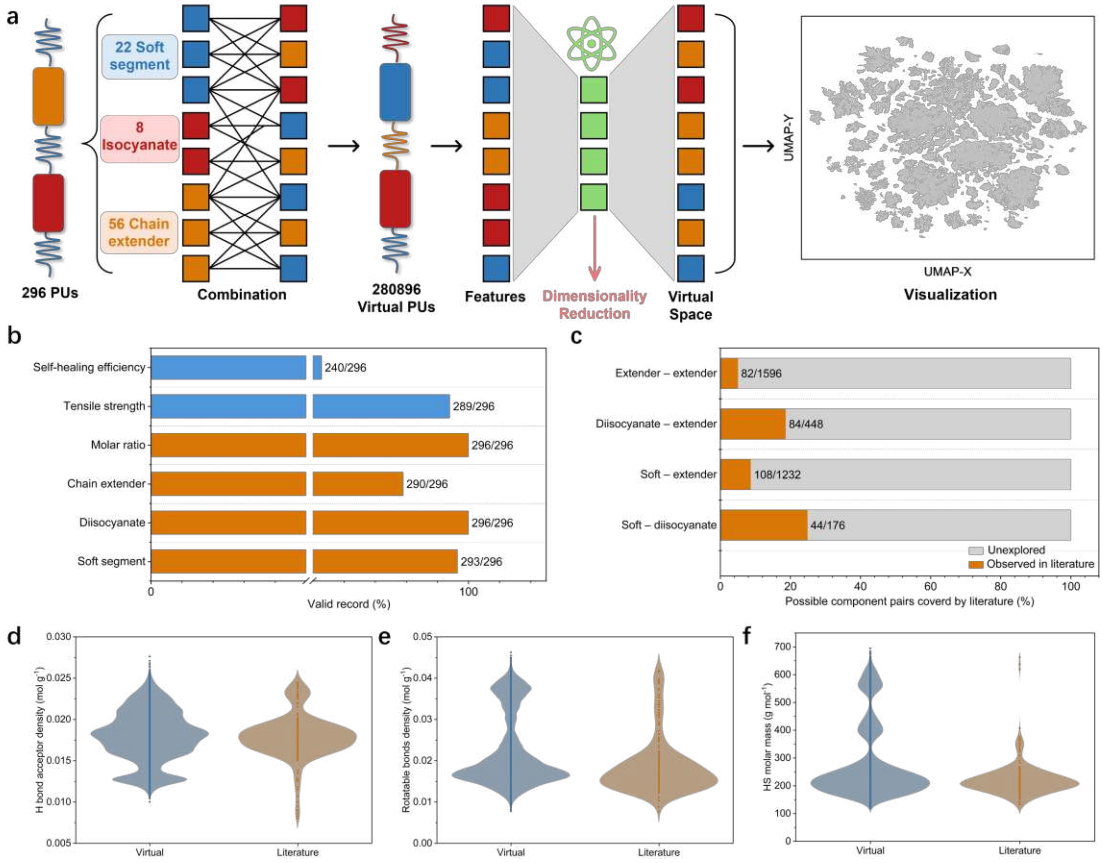


Fig. 2 | Construction of the formulation representation for polyurethane elastomers. a Schematic illustration of the workflow from monomer combinations to dimensionality reduction. **b** Fraction of literature records with valid values for each formulation or performance field. **c** Coverage of component-pair combinations by the literature formulations. **d-f** Distributions of hard-segment (HS) H-bond acceptor density (mol g^{-1}), HS rotatable-bond density (mol g^{-1}), and HS mean molar mass (g mol^{-1}), respectively.

A common representation was built from 13 structural and compositional descriptors drawn from polymer-informatics and materials-discovery practice. The descriptor selection principle was that a formulation map should retain chemically interpretable information about component identity, size, polarity, hydrogen-bonding capacity, flexibility, and composition while excluding redundant variables. Reviews of molecular descriptors provide precedents for combining molecular, topological, and composition-derived features in polymer design[32]. Polyurethane-specific machine-learning studies have examined multicomponent elastomer properties, mechanical response, acoustic

coatings, and glass-transition behavior[24,33-35]. Chemical-language models, ionic-polymer studies, and simulation-derived ion-transport descriptors provide complementary representation examples[21,25,36], while rule-based polymer libraries support systematic enumeration[37]. Additional formulation-level context is provided by studies on tough polymers and self-healing mechanisms[38-40]. These descriptors capture differences in intermolecular association, conformational freedom, molecular size, charge distribution, and molecular shape, enabling consistent application to both literature and virtual entries. **Fig. 2**d-f presents distributions of H-bond acceptor density, HS rotatable-bond density, and HS mean molar mass, respectively. The virtual library overlaps the literature-supported domain while extending into combinations absent from the 296 anchors, thereby creating an anchor-guided map for prioritization. Morphology and processing history remain experimental dimensions represented only indirectly at this stage, and the descriptor set was intentionally formulation-centered to maximize coverage across the heterogeneous literature. Component identity and molecular size distinguish the chemical building blocks; polarity and hydrogen-bonding terms capture the likely intermolecular association; and flexibility and composition terms describe how the blocks are combined. This balance yields a first-pass map with chemically readable axes that is not dominated by any single molecular substructure. Visual assessment and descriptor distribution diagnostics confirmed overlap between literature and virtual entries prior to clustering, verifying that the virtual library remains connected to empirical anchors. Descriptor correlation and distribution diagnostics are provided in Supplementary Figs. S2-S15 and Supplementary Tables S4 and S5.

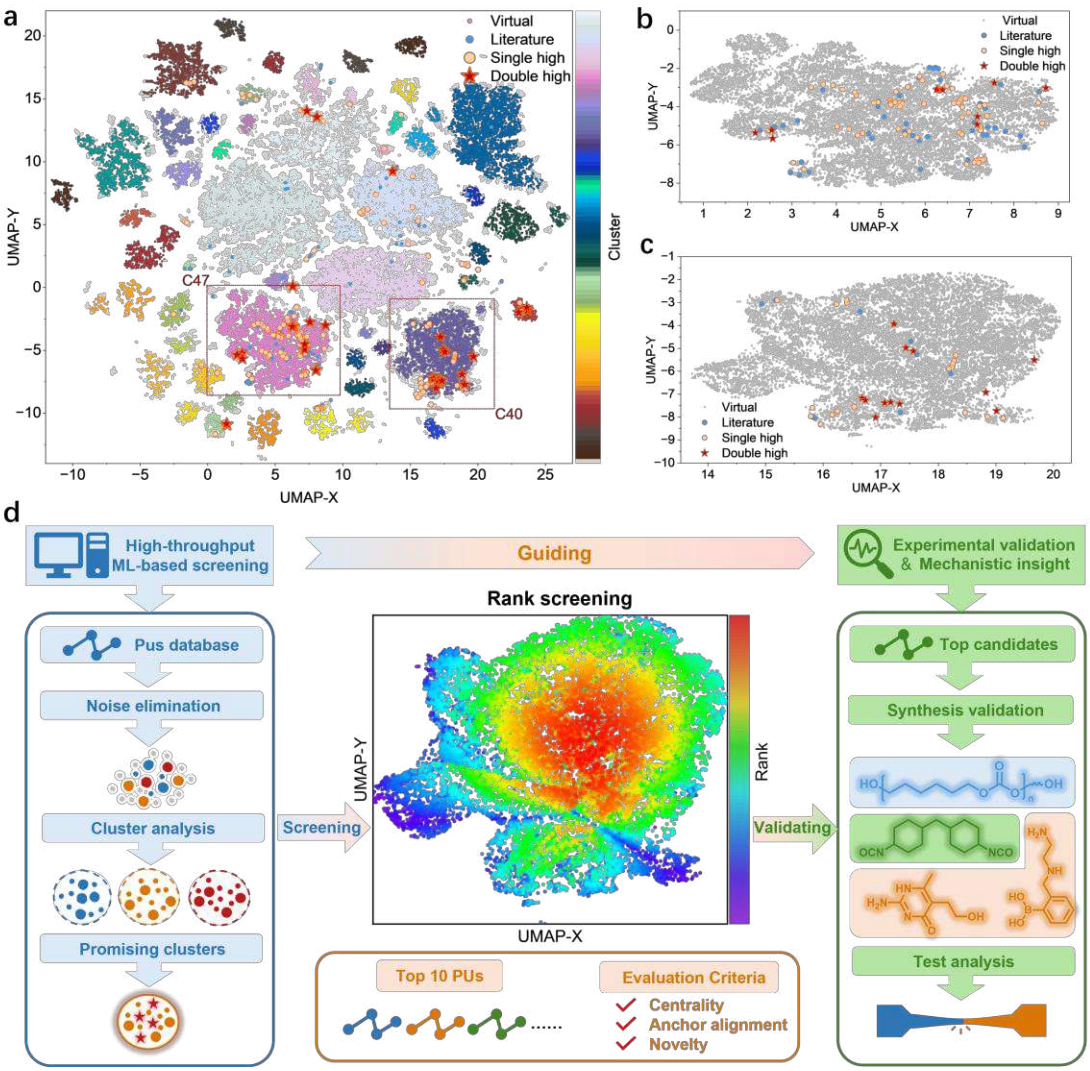


Fig. 3 | Unsupervised clustering and candidate prioritization within polyurethane formulation space. a UMAP projection and HDBSCAN clustering results. **b,c** Intra-cluster distributions of Clusters C47 and C40. Anchor symbols in a-c retain the experimental-selection classifications; **d** Candidate prioritization workflow from cluster selection and geometric ranking to synthesis and experimental testing.

Anchor counts define exploratory prioritization regions

Following standardization, UMAP mapped local neighborhood relations into two dimensions, and HDBSCAN separated density-connected regions, yielding 57 clusters and 53,975 noise points. **Fig. 3**a presents the shared chemical-space map and its density-based partition, where cluster labels define chemically coherent neighborhoods for candidate inspection. **Fig. 3**b,c compares the anchor composition of C47 and C40, illustrating the distribution of double-high, single-high, and ordinary literature

formulations alongside virtual formulations in each region. This sequence links representation, clustering, and candidate inspection in a single reproducible workflow[41,42]. The shared projection is shown in Supplementary Fig. S16. Embedding sensitivity is examined in Supplementary Figs. S17 and S18, while the reference partition and its density-parameter sensitivity appear in Supplementary Fig. S19 and Supplementary Figs. S20-S22, respectively.

The literature anchors supplied the initial performance screen. An anchor is labeled double-high when its tensile strength is >20 MPa, and its healing efficiency is >0.90; satisfying exactly one threshold gives a single-high label. C40 contains 18,686 virtual formulations and 38 external literature anchors, including 12 double-high, 18 single-high, and 8 ordinary anchors, the largest absolute number of double-high anchors among the 57 non-noise clusters. C47 contains 24,494 virtual formulations and 118 external literature anchors, including 10 double-high, 64 single-high, and 44 ordinary anchors under the classifications used for candidate selection. C40 was retained as the primary prioritization region, whereas C47 served as a distinct comparison neighborhood. The original experimental-selection queues retain their reported reference classifications. The retained-region sizes and anchor compositions are summarized in Supplementary Fig. S23.

These two retained regions narrowed the enumerated virtual library from 280,896 to 43,180 candidate formulations while preserving a direct link to literature anchors. Each retained formulation could be traced to its component combination, descriptor vector, and position in the UMAP representation. This traceability enabled inspection of structural plausibility and synthetic accessibility for each candidate prior to synthesis selection.

Geometry-based ranking defines the experimental candidate queue

Cluster membership alone left 43,180 virtual formulations to be ranked, and three complementary geometric criteria were used. E1 (Centrality) favored points near the cluster centroid, rewarding formulations at the structural core of a chemically coherent region. E2 (Anchor alignment) measured alignment between each candidate's displacement from the mean of its nearest double-high anchors and their principal axis in the UMAP plane. E3 (Novelty) combined the mean distance to nearby scoring references in standardized descriptor space with a Gaussian weight centered on the regional mean distance, balancing structural novelty with local reference support. Their geometric mean defines the within-region order so that Centrality, Anchor alignment, and Novelty are considered jointly rather than independently. Score components and ranking stability are shown in Supplementary Figs. S24-S29, and the definitions and regional queues are given in Supplementary Methods SM8a and Supplementary Tables S9 and S10.

The ten highest-ranked virtual candidates from each region were retained for detailed inspection (**Fig. 3**d). They were evaluated against three additional criteria: (i) structural plausibility (whether the component combination is chemically consistent with known polyurethane synthesis); (ii) reagent availability (whether all monomers are commercially obtainable or synthesizable via established routes); and (iii) synthetic accessibility (whether the formulation can be prepared by conventional step-growth polymerization without specialized equipment). The practical screen retained three formulations from each regional Top-10 queue, yielding six candidates for synthesis and experimental comparison. These included the C40 rank-10 PC2000/HMDI/UPy/PBA formulation, which combined a commercially available polycarbonate soft segment (PC2000) and aliphatic diisocyanate (HMDI) with two

well-established dynamic motifs, UPy quadruple hydrogen bonding and PBA-derived dynamic boroxine formation, whose synergistic interplay had not been systematically explored in this formulation context. The paired tensile measurements identified this formulation as the strongest of the six candidates both before and after healing. It is denoted PUUB throughout: PU for the polyurethane backbone, U for the UPy-containing chain-extending unit, and B for the PBA-derived terminal unit. The design stoichiometry was PC:HMDI:UPy:PBA = 2:4:1:2. PUU and PUB were prepared as chemically simpler controls to separate the individual contributions of the UPy extender and the PBA-derived component in subsequent characterization. The transition from regional queues to the six candidates is shown in Supplementary Figs. S30 and S31, and their stress-strain responses and paired peak values are provided in Supplementary Figs. S33, S34, and Table S13.

The candidate queue defined the experimental case study. C40 and C47 supplied the candidate neighborhoods, E1-E3 supplied the reproducible geometric order, and the three-step plausibility-availability-accessibility filter led to six formulations for synthesis and experimental comparison, from which PUUB was selected. **Fig. 3**d records the progression from high-throughput screening to candidate selection and comparative experimental evaluation. The subsequent PUUB, PUU, and PUB experiments tested the selected chemistry and separated the effects of the two dynamic formulation components.

Structural and physicochemical characterization of PUUB and formulation controls

The candidate comparison identified PC2000/HMDI/UPy/PBA as the formulation for detailed experimental evaluation (**Fig. 4**a,b), denoted PUUB. PUU and PUB retained the same PC2000-HMDI backbone while using UPy or PBA as the sole dynamic

component, enabling a controlled decomposition of their individual and synergistic contributions. The PUUB synthesis scheme, intermediate syntheses, and NMR characterization are shown in Supplementary Figs. S35-S37.

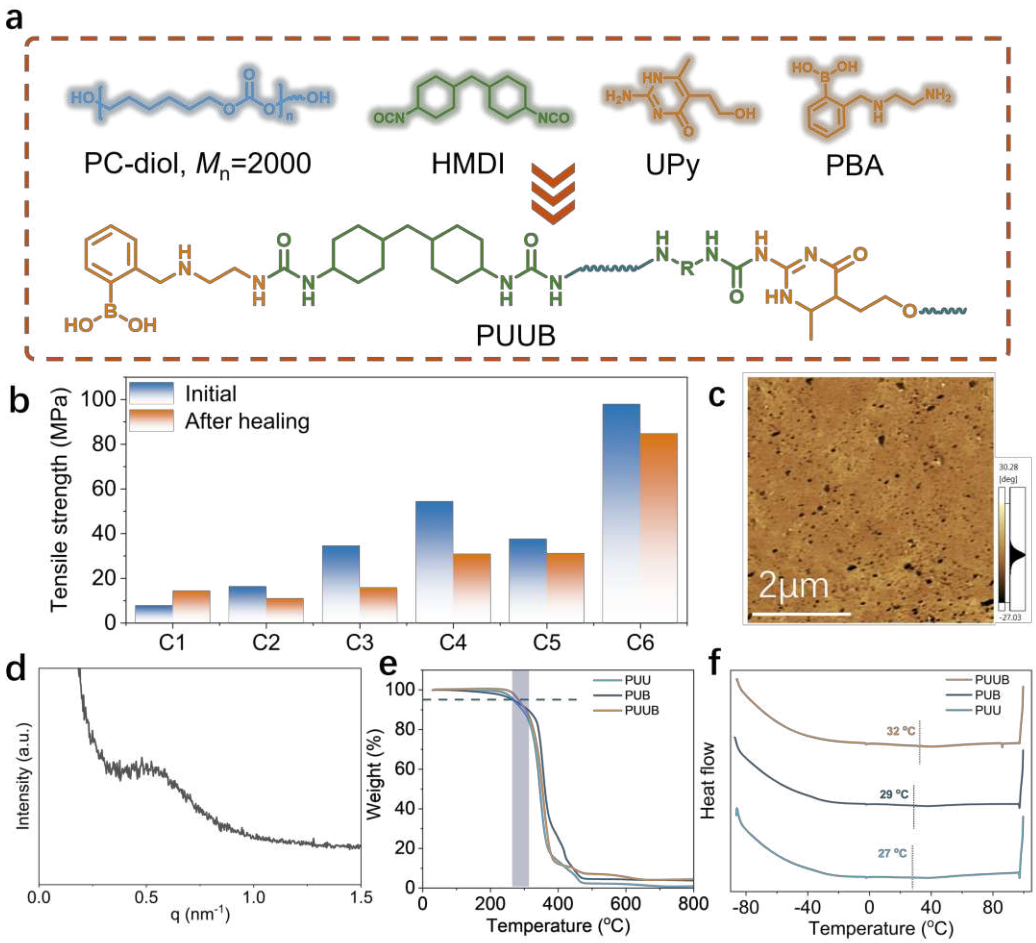


Fig. 4 | Chemical structure, candidate performance comparison, and physicochemical characterization of PUUB, PUB, and PUU. a Formulation structures and the bifunctional molecular skeleton of PUUB. **b** Initial and post-healing tensile strengths of the six candidate formulations (C1–C6); C6 is PUUB. **c** AFM phase image of the PUUB surface morphology. **d** SAXS pattern of PUUB. **e** TGA curves. **f** DSC curves of PUUB, PUB, and PUU.

The Fourier-transform infrared (FTIR) spectra confirm the common urethane framework of all three materials (Supplementary Fig. S38). PUB and PUUB additionally display aromatic-ring skeletal vibrations in the 1450-1620 cm^{-1} region and a boroxine-ring vibration near 682 cm^{-1}, consistent with incorporation of the PBA-derived component and the formation of dynamic boroxine crosslinks. The ^{1}H NMR

spectra provide complementary molecular-level assignments (Supplementary Fig. S39): PUU shows the UPy-related signal at 8.05 ppm together with the 6.34-6.92 ppm signals associated with UPy and urethane protons, whereas PUB and PUUB show signals at 6.64, 6.94, and 7.74 ppm assigned to urethane and urea protons formed in the PBA-HMDI chemistry, with aromatic PBA protons at 7.19-7.61 ppm. Signals at 1.29 and 1.56 ppm arise from alkyl protons, and the 4.07 ppm signal is assigned to PC alkoxy-related protons. Together, the FTIR and ^{1}H NMR data identify the expected chemical signatures in PUU, PUB, and PUUB and confirm the successful incorporation of both dynamic motifs in PUUB.

The atomic force microscopy (AFM) image of PUUB visualizes distinct surface domains with nanoscale compositional contrast (**Fig. 4**c), supporting the presence of phase separation at the imaged scale. The small-angle X-ray scattering (SAXS) pattern resolves the microphase-separated length scale of PUUB (**Fig. 4**d). For PUUB, the position of the principal scattering maximum, q*, was used to estimate the corresponding characteristic domain spacing through $d = 2\pi/q^*$. PUUB exhibits a well-defined scattering maximum consistent with a periodic microphase-separated morphology, in which the UPy- and boroxine-rich hard domains are dispersed within a continuous PC2000 soft matrix. The thermogravimetric analysis (TGA) curves record the thermal decomposition profiles (**Fig. 4**e), with all three formulations showing a decomposition onset above 250 °C, adequate for the intended application range. The differential scanning calorimetry (DSC) traces distinguish their thermal transitions (**Fig. 4**f): PUUB shows a glass transition near 32 °C, slightly higher than PUB (29 °C) and substantially higher than PUU, reflecting the additional physical crosslinking imposed by the combined UPy-boroxine network. These AFM, SAXS, TGA, and DSC observations establish the structural and thermal context for the mechanical response:

the microphase-separated morphology provides both reinforcing hard domains and a continuous soft phase for extensibility, while the dual dynamic motifs enable reversible energy dissipation and bond reconfiguration. The role of morphology in segmented polyurethane and polyurea properties has been reviewed previously[43]. Additional SAXS and AFM morphology analyses are provided in Supplementary Figs. S40-S43.

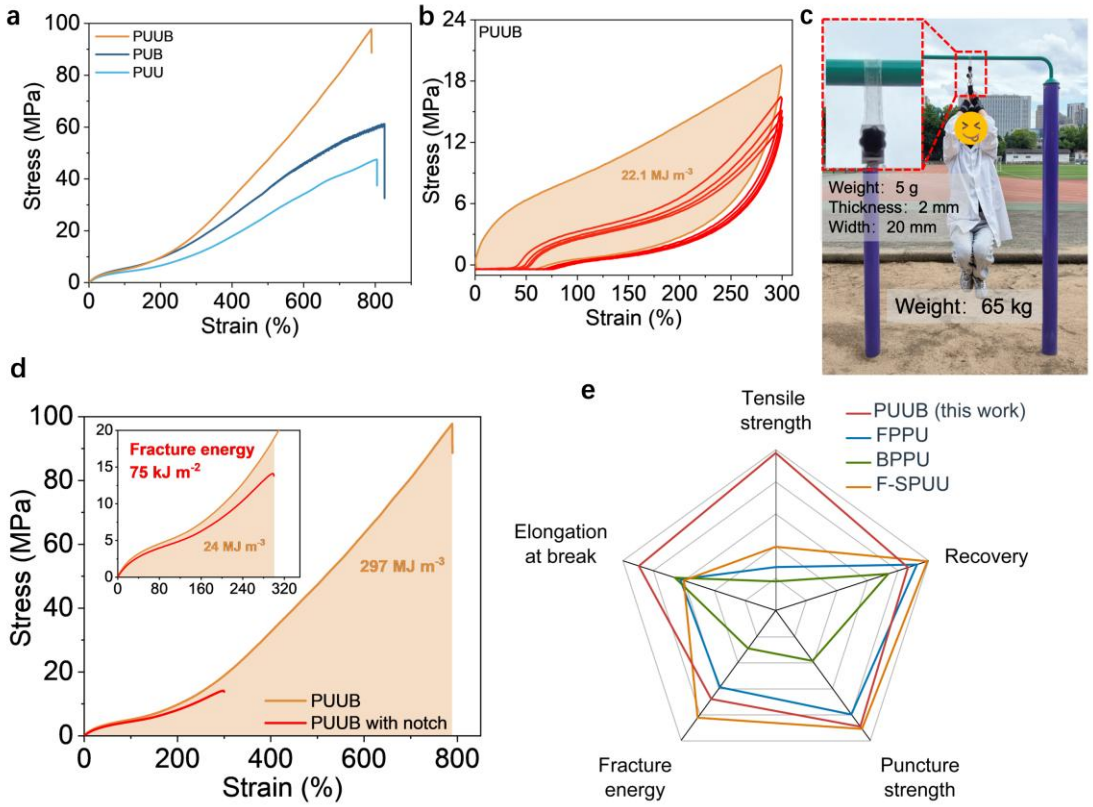


Fig. 5 | Mechanical performance and damage tolerance of PUUB. a Tensile test of PUUB, PUB, and PUU. **b** Cyclic tensile loading-unloading responses of PUUB. **c** Practical load-bearing demonstration in which a 5 g PUUB accessory supports a 65 kg person. **d** Tensile stress-strain curves of pristine and notched PUUB; the inset highlights the notched response and the corresponding fracture energy. **e** Five-property radar comparison of PUUB with FPPU and BPPU from Jia et al.[44] and F-SPUU from Jia et al.[45]. The axes represent tensile strength, tensile-strength recovery after healing, thickness-normalized puncture strength, fracture energy, and elongation at break. Literature source values and test conditions are provided in Supplementary Table S15.

PUUB sustained the highest stress among the three materials across the entire strain regime, reaching approximately 98 MPa at 788% elongation (**Fig. 5**a) with a tensile work-to-fracture of approximately 297 MJ m^{-3}. By comparison, PUB reached

approximately 62 MPa and PUU approximately 48 MPa at comparable elongations. The substantial performance gap between PUUB and either single-component control is consistent with synergistic interplay between the two dynamic motifs: the UPy quadruple hydrogen bonds provide strong, directional physical crosslinks that reinforce the hard domains and bear load at high strains, while the PBA-derived boroxine motifs offer dynamic covalent exchange that facilitates stress redistribution and prevents catastrophic crack propagation. Neither motif alone achieves this combination: PUU lacks the dynamic covalent pathway for efficient stress relaxation, and PUB lacks the strong hydrogen-bonding array for high load-bearing capacity. The separation of the three curves across the high-strain region therefore validates the design logic that motivated the dual-motif PUUB formulation. The response to UPy-content variation is documented separately in Supplementary Fig. S44.

PUUB also performed well under cyclic and notched loading. The first loading-unloading loop enclosed approximately 22.1 MJ m^{-3} (**Fig. 5**b), indicating substantial energy dissipation during extension and recovery consistent with reversible UPy hydrogen-bond rupture and boroxine exchange acting as sacrificial bonds. Subsequent cycles showed progressively smaller hysteresis, consistent with the gradual re-equilibration of the dynamic network. A 5 g loading accessory was used to suspend a 65-kg person (**Fig. 5**c), providing a macroscopic demonstration of the material's load-bearing capacity. In the notched test (**Fig. 5**d), the stress-strain response gave an integrated work-to-fracture of approximately 24 MJ m^{-3} under a defined 1 mm partial cut, corresponding to a fracture energy of approximately 75 kJ m^{-2}. The notched specimen did not fail immediately at the notch tip but instead underwent extensive plastic drawing before fracture (Supplementary Fig. S45 and Supplementary Video), indicating that the dynamic network effectively blunts cracks and redistributes stress

through bond exchange.

The radar profile in **Fig. 5**e places this mechanical response alongside three strong, healable polyurethane-based elastomers: FPPU and BPPU from the same study[44], and F-SPUU from a separate study[45]. PUUB combines approximately 98 MPa tensile strength and 788% elongation at break, compared with 26.98 MPa and 550% for FPPU, 18.07 MPa and 580% for BPPU, and 39.6 MPa and approximately 530% for F-SPUU. Its approximately 75 kJ m^{-2} fracture energy and 98.37 N mm^{-1} puncture strength accompany 86.5% tensile-strength recovery, establishing a performance profile in which high load-bearing capacity and large deformation coexist with damage resistance and repair. The pronounced strength-extensibility combination reflects the cooperation of reinforcing UPy associations, the extensible polycarbonate matrix, and the PBA-derived dynamic junctions. The healing response underlying the recovery axis is examined in **Fig. 6**.

The structural characterization and mechanical tests together establish the combination of high strength, extensibility, and notch tolerance in PUUB. Related polyurethane elastomers have reported mechanical robustness and crack tolerance using hydrogen-bond arrays and hierarchical associations[46-48]. Polyurethane ionogels and ion-conductive elastomers further extend dynamic-network design to functional materials[49,50]. Hindered urea and boronic ester networks tune toughness, healing, reprocessing, and adhesion[51-53], while microphase separation strengthens reversible epoxy-polyurethane adhesives[54]. Phase-locked and water-insensitive elastomers illustrate further healing strategies[55,56]. Dynamic disulfide and hierarchical hydrogen-bonded networks provide additional reinforcement and recovery pathways[57,58]. Shi and co-workers have also constructed polymer electrolytes with dynamic covalent networks by initiator-free thiol-methacrylate polymerization[59]. Related work from the group

combines urea hydrogen bonding with disulfide metathesis in a self-healing electrolyte matrix[60] and uses boronic ester networks for self-healing and recyclable polymer electrolytes[61,62].

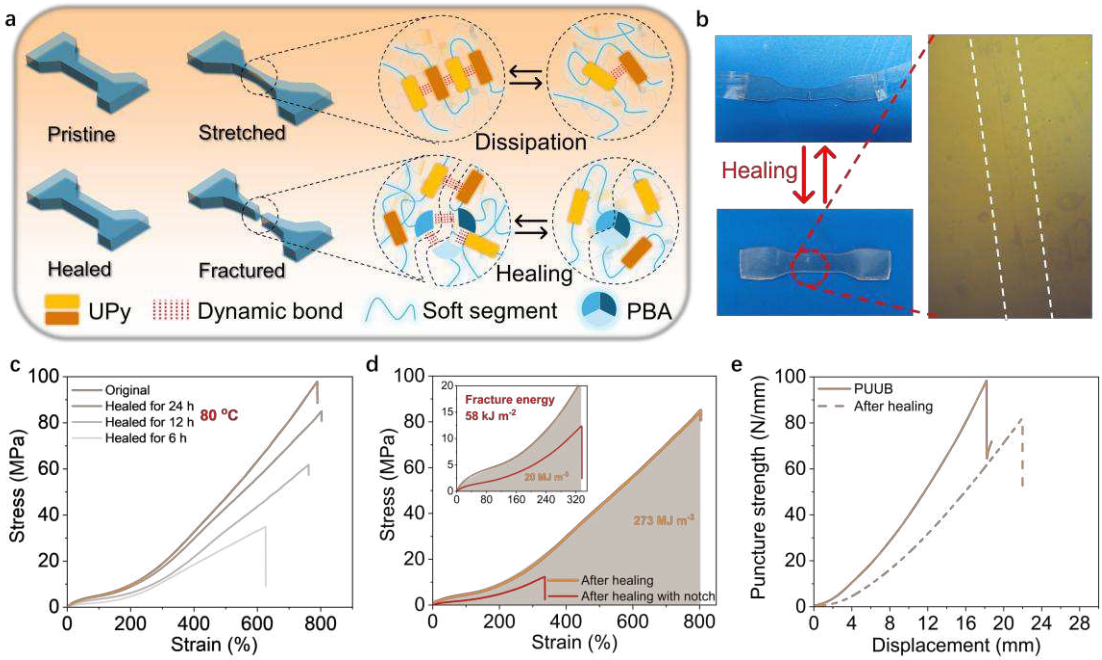


Fig. 6 | Hierarchical dissipation mechanism and self-healing performance of PUUB. **a** Proposed molecular mechanism linking hierarchical energy dissipation during stretching to network reconstruction through reversible hydrogen bonding and PBA-derived boroxine junctions. **b** Macroscopic photographs before and after healing and an optical micrograph of the healed cut region. **c** Tensile stress-strain curves of pristine PUUB and specimens healed at 80 °C in the presence of water for 6, 12, and 24 h after a four-fifths-width cut. **d** Tensile stress-strain curves of healed PUUB with and without a notch; the inset highlights the notched response and the fracture energy after healing. **e** Thickness-normalized puncture strength-displacement curves of PUUB before and after healing.

The molecular picture in **Fig. 6**a provides a common explanation for energy dissipation and interfacial reconstruction. We propose a hierarchy in which relatively labile urethane- and urea-associated hydrogen bonds open first, allowing soft-segment extension and local chain rearrangement; the stronger UPy quadruple-hydrogen-bond arrays then sustain and redistribute larger loads, while reconfiguration of the PBA-derived boroxine junctions provides an additional route for network relaxation. Distributed bond rupture and reassociation spread the deformation over a broad region

around a defect, linking the cyclic hysteresis to crack blunting. During healing, heating increases segmental mobility, and water promotes reversible hydrolysis of the six-membered boroxine rings to boronic-acid groups. The healing mechanism involves two complementary processes: at the cut interface, quadruple hydrogen bonds reassociate across the newly contacted surfaces, providing rapid initial cohesion, while the PBA-derived boroxine bonds undergo dynamic covalent exchange at elevated temperature, enabling interfacial polymer chain diffusion and the re-establishment of a covalently connected network.

For healing evaluation, we manually realigned a four-fifths-width cut and heated it at 80 °C in the presence of water for 6, 12, or 24 h. The cut region progressively closed during treatment, and the PUUB fracture-strength recovery increased with healing time to 86.5% after 24 h (**Fig. 6**b,c). Healed specimens recovered a continuous load-bearing path across the deep partial cut, complementing the tensile and notch measurements by showing that the same formulation can restore load transfer after severe damage. A healed specimen also supported a 5 kg load (Supplementary Fig. S46), illustrating the recovery of macroscopic load-bearing capacity after healing.

Recovery extends from uniaxial strength to resistance against renewed local damage. The healed, unnotched PUUB response integrates to approximately 273 MJ m^{-3}, while the healed notched specimen retains approximately 20 MJ m^{-3} of work-to-fracture and a fracture energy of approximately 58 kJ m^{-2} (**Fig. 6**d). The latter corresponds to approximately 77% of the pristine value of 75 kJ m^{-2}, showing that network reconstruction restores a substantial capacity to dissipate energy around a crack. The puncture curves provide a complementary test of concentrated loading (**Fig. 6**e): the healed specimen reaches approximately 80 N mm^{-1} compared with approximately 98 N

mm^{-1} before healing, while accommodating a larger displacement before penetration. Re-established hydrogen-bond arrays and boroxine junctions therefore recover both interfacial cohesion and distributed load transfer, allowing the repaired material to resist tensile, crack-opening, and puncture loads.

Discussion

This study addresses a practical challenge in polymer discovery: literature measurements are often difficult to compare, even when formulations are described in detail. An unsupervised representation can organize these records for candidate selection without treating reported properties as directly comparable training labels. We mapped 296 literature formulations and 280,896 virtual combinations into a shared space defined by 13 descriptors. UMAP dimensionality reduction and HDBSCAN clustering identify chemically coherent neighborhoods, and the number of double-high literature anchors (strength >20 MPa, healing >0.90) provides an empirical basis for regional prioritization. Three geometric scores (E1-E3) ranked candidates within the retained regions. We provide formulation records, descriptor values, reported mapping outputs, and regional scoring code to enable inspection of the workflow and reproduction of the regional ranking stage.

The mechanical response of PUUB reflects interactions across molecular, microstructural, and macroscopic scales. At the molecular level, quadruple hydrogen bonds provide strong, directional, and reversible physical crosslinks that reinforce the hard domains, while PBA-derived boroxine rings offer a complementary covalent exchange pathway. SAXS and AFM reveal microphase-separated domains within a continuous PC2000 soft matrix, consistent with the coexistence of extensibility and load-bearing hard domains. Macroscopically, PUUB achieves a tensile strength of 98

MPa, dissipates 22.1 MJ m^{-3} in the first loading cycle, exhibits a fracture energy of 75 kJ m^{-2}, and recovers 86.5% of its fracture strength after healing at 80 °C in the presence of water. The single-motif controls, PUU and PUB, lack one of these pathways and show inferior performance, consistent with a synergistic contribution from combining both motifs. The healed material also retains approximately 58 kJ m^{-2} fracture energy and approximately 80 N mm^{-1} puncture strength, extending recovery from tensile strength to resistance against localized damage.

This approach may apply to other materials systems where literature records contain detailed structural information but inconsistent measurements. The unsupervised map relies on structural descriptors that are uniformly available across all formulations, while reported properties guide anchor selection rather than serving as harmonized regression targets. The number of double-high literature anchors then provides an empirical basis for regional prioritization, although anchor selection remains dependent on reported measurement conditions. The method can be adapted to polymer families in which dynamic bonds, phase separation, and composition jointly influence performance. Future studies could incorporate experimental results into the ranking and update candidate priorities as new formulations are tested.

Methods

Literature data, virtual-library construction, and descriptors

The literature database contained 296 polyurethane formulations curated from peer-reviewed publications on self-healing and mechanically robust polyurethane elastomers. The virtual library was enumerated from 22 soft segments, eight diisocyanates, and 56 chain extenders. Unordered chain-extender pairs with repetition produced 1,596 pairings and hence 280,896 virtual formulations. Molecular and composition-derived

descriptors were calculated from component SMILES using the project scripts. Descriptor construction followed established polymer informatics practice, in which complementary molecular, topological, and composition features are combined before dimensionality reduction[32-35,37]. Low-variance filtering (VarianceThreshold = 0.02) and high-correlation filtering (absolute correlation threshold = 0.8) were applied during preprocessing. The final working representation was selected before experimental synthesis to avoid selection bias. The formulation library comprises 281,192 records, including 280,896 virtual formulations and 296 external literature records (Supplementary Methods SM1–SM5).

Chemical-space mapping, clustering, and ranking

The 13 descriptors were standardized with StandardScaler and embedded with UMAP using n_components = 2, n_neighbors = 30, min_dist = 0.5, Euclidean metric, and random_state = 42. HDBSCAN was applied to the UMAP coordinates with min_cluster_size = 200, min_samples = 400, and Euclidean metric. A literature formulation is labeled double-high when its tensile strength is >20 MPa, and its healing efficiency is >0.90; a formulation meeting exactly one threshold is labeled single-high. These labels are used to inspect anchor patterns. C40 contains the largest absolute number of double-high anchors among the non-noise clusters and was retained as the primary prioritization region; C47 was retained as a distinct comparison neighborhood. Within each cluster, E1, E2, and E3 were combined by their geometric mean. The implementation sets K2 = 11 and M = 11, caps the double-high neighborhood at the number available, discards the closest scoring-reference neighbor for every query, and assigns score ranks over all regional rows. The reported Top-10 queues contain virtual formulations. The formulation library contains 281,192 records (280,896 virtual formulations plus 296 external literature formulations). Experimental-selection scores

and reference classes are preserved in Supplementary Data 06 and 07. Formulas, normalization, and boundary handling are given in Supplementary Methods SM8-SM8a and the experimental-selection queues in Supplementary Tables S9 and S10.

Materials and formulation preparation

PC2000 polycarbonate diol (UBE Chemicals) and 4,4′-dicyclohexylmethane diisocyanate (HMDI; Macklin) were used as the soft segment and diisocyanate, respectively. The bifunctional ureidopyrimidinone (UPy) chain extender and terminal aliphatic monoaminophenylboronic acid (PBA) end-capping reagent were synthesized according to the cited procedures[63,64]. The formulation PC2000/HMDI/UPy/PBA is denoted PUUB; PUU contains UPy without PBA, and PUB contains PBA without UPy. For UPy synthesis, 2-acetylbutyrolactone and guanidine carbonate (40 mmol each) were dispersed in anhydrous ethanol (40 mL), followed by triethylamine (80 mmol). The mixture was refluxed at 90 °C for 6 h; the isolated solid was washed once with deionized water and three times with ethanol, then dried under vacuum at 60 °C for 24 h. PBA was prepared from 2-formylphenylboronic acid (20 mmol) and *N*-Boc-ethylenediamine (25 mmol) in methanol (30 mL). After addition of triethylamine (2 mL) at 0-8 °C, the mixture was stirred for 1 h at 0-8 °C and 24 h at room temperature. Sodium borohydride (30 mmol) was added portionwise in an ice bath, and the mixture was stirred for a further 6 h. Methanol was removed, the product was dissolved in dichloromethane (200 mL), washed with saturated brine three to five times, redissolved in methanol (50 mL), and treated with HCl (20 mmol) in an ice bath to remove the Boc group. The product was dried under vacuum at 80 °C for 24 h.

Film casting, curing, and specimen conditioning

For PUUB synthesis, PC2000 (5 mmol) was dried under reduced pressure at 100 °C for 1-2 h. After cooling to 60 °C, the polyol was dissolved in anhydrous *N,N*-

dimethylformamide (DMF; 40 mL), and HMDI (10 mmol) and 2-3 drops of dibutyltin dilaurate were added. The mixture was reacted under nitrogen at 60 °C for 6 h. UPy (2.5 mmol) was then added, and the reaction continued at 80 °C for 6 h. After cooling to 30 °C, PBA (8 mmol) was added, and the reaction continued for 12 h. The design stoichiometry of PC:HMDI:UPy:PBA was 2:4:1:2; PBA was supplied in excess in the preparative batch to drive the terminal reaction to completion, while the stated design stoichiometry describes the intended reacting groups. The polymer solution was precipitated by dropwise addition into vigorously stirred deionized water, redissolved in a small amount of DMF, and reprecipitated in water three times. PUU used UPy as the sole chain-extending component and contained no PBA. PUB used PBA as the sole chain-extending/end-capping component and contained no UPy. Films were cast in polytetrafluoroethylene molds (approximately 5 cm in radius and 2 cm in depth) and cured in a forced-air oven at 80 °C overnight. Specimens were trimmed to 20 mm length and 2 mm width before testing; thickness varied between specimens and was measured for stress calculation.

Spectroscopy, thermal analysis, and morphology

FTIR spectra were acquired on a Bruker Equinox 55 over 500-4000 cm^{-1} at the instrument's default resolution. ^{1}H NMR spectra were recorded on a Bruker AV400 spectrometer using DMSO-d_6 as the solvent. The SAXS pattern shown in **Fig. 4**d was used for structural characterization of PUUB. The SAXS profile reduction and AFM image-scale analysis are described in Supplementary Methods SM11b. In PUU, signals at 8.05 ppm and 6.34-6.92 ppm were assigned to UPy- and urethane-related protons. In PUB and PUUB, signals at 6.64, 6.94, and 7.74 ppm were assigned to urethane and urea protons associated with the reaction of PBA and HMDI, and aromatic PBA protons occurred at 7.19-7.61 ppm. Signals at 1.29 and 1.56 ppm were assigned to alkyl protons,

and the signal at 4.07 ppm to PC alkoxy-related protons. In the FTIR spectra of PUB and PUUB, bands at 1450-1620 cm^{-1} and 682 cm^{-1} were assigned to aromatic-ring skeletal vibrations and boroxine-ring vibrations, respectively. These assignments are formulation-level evidence for the intended chemical structures. DSC was performed on a Q2000 at 10 °C min^{-1}. TGA was performed on a PerkinElmer 4000 under nitrogen. AFM images were acquired using a Shimadzu SPM-9700 to visualize surface morphology; PUUB fields were analyzed by phase-image autocorrelation as described in Supplementary Methods SM11b.

Mechanical testing

Uniaxial tensile tests were performed at room temperature on a UTM2103 universal testing machine at 50 mm min^{-1}. Specimens were 20 mm long and 2 mm wide, and thickness varied between specimens. Engineering stress was calculated from force divided by the specimen-specific initial cross-sectional area. Puncture responses before and after healing were measured at 10 mm min^{-1}, with force normalized by specimen thickness and reported in N mm^{-1}. Healed specimens were additionally evaluated by notched tensile loading to assess their resistance to renewed crack opening.

Notched tensile work-to-fracture

The geometry-specific notched tensile work-to-fracture was measured at room temperature. A notch of approximately 1 mm, corresponding to one-half of the specimen width, was introduced with scissors. The stress-strain response was integrated from zero to the fracture point. The test used the tensile conditions described above and was intended to compare resistance to failure after a defined partial cut.

Healing evaluation

Healing specimens were cut to approximately 1.6 mm, corresponding to four-fifths of the specimen width, with scissors. The cut surfaces were manually realigned, covered

with a glass plate, and secured with small clips at both sides. The aligned specimens were heated at 80 °C in the presence of water for 6, 12, or 24 h. Recovery was calculated as the healed fracture strength divided by the corresponding original fracture strength, multiplied by 100. The healing experiment used a deep partial cut to permit re-contact and assess structural recovery, whereas the notch test used a 1 mm cut to evaluate crack tolerance in the as-prepared material.

Data availability

All machine-readable data supporting the findings are provided in the accompanying supplementary data package. OriginData contains the processed numerical data used to generate the figures and tables. Component_Inventory.xlsx provides the component identities and SMILES mapping, Literature_Formulations.xlsx provides the external literature formulation and property records, and Literature_DOI_Mapping.xlsx provides the corresponding DOI and source links. Origin project files and raw instrument files are not included in the release package. The literature-formulation and component-structure input workbooks are also available in the GitHub release cited under Code availability.

Code availability

The code for virtual-formulation enumeration, ratio representation, descriptor calculation, UMAP embedding, HDBSCAN clustering, and regional candidate scoring is publicly available on GitHub (release v0.1.0-rc.1): https://github.com/mine12138-xx/polyurethane-data-code/releases/tag/v0.1.0-rc.1. The release includes the input workbooks OriginData.xlsx and SMILES.xlsx, workflow documentation, and dependency specifications.

References

1. Huang, Y. et al. Shape-memory and self-healing polyurethane-based solid polymer electrolytes constructed from polycaprolactone segment and disulfide metathesis. Energy Storage Mater. 51, 1-10 (2022). https://doi.org/10.1016/j.ensm.2022.06.021

2. Huang, Y. et al. Disulfide bond-embedded polyurethane solid polymer electrolytes with self-healing and shape-memory performance. Polym. Chem. 13, 6002-6009 (2022). https://doi.org/10.1039/D2PY00944G

3. Cordier, P., Tournilhac, F., Soulie-Ziakovic, C. & Leibler, L. Self-healing and thermoreversible rubber from supramolecular assembly. Nature 451, 977-980 (2008). https://doi.org/10.1038/nature06669

4. Sijbesma, R. P. et al. Reversible polymers formed from self-complementary monomers using quadruple hydrogen bonding. Science 278, 1601-1604 (1997). https://doi.org/10.1126/science.278.5343.1601

5. Eom, Y. et al. Mechano-responsive hydrogen-bonding array of thermoplastic polyurethane elastomer captures both strength and self-healing. Nat. Commun. 12, 621 (2021). https://doi.org/10.1038/s41467-021-20931-z

6. Xu, J., Chen, J., Zhang, Y., Liu, T. & Fu, J. A fast room-temperature self-healing glassy polyurethane. Angew. Chem. Int. Ed. 60, 7947-7955 (2021). https://doi.org/10.1002/anie.202017303

7. Wang, X. et al. Healable, recyclable, and mechanically tough polyurethane elastomers with exceptional damage tolerance. Adv. Mater. 32, 2005759 (2020). https://doi.org/10.1002/adma.202005759

8. Yao, Y. et al. Multiple H-bonding chain extender-based ultrastiff thermoplastic polyurethanes with autonomous self-healability, solvent-free adhesiveness, and AIE fluorescence. Adv. Funct. Mater. 31, 2006944 (2021). https://doi.org/10.1002/adfm.202006944

9. Guo, Z. et al. Engineering of chain rigidity and hydrogen bond cross-linking toward ultra-strong, healable, recyclable, and water-resistant elastomers. Adv. Mater. 35, 2300286 (2023). https://doi.org/10.1002/adma.202300286

10. Zhu, X. et al. Ultrahigh mechanical strength and robust room-temperature self-healing properties of a polyurethane-graphene oxide network resulting from multiple dynamic bonds. ACS Nano 16, 16724-16735 (2022). https://doi.org/10.1021/acsnano.2c06264

11. Wang, X. et al. Self-healing polyurethane elastomers with superior tensile strength and elastic recovery based on dynamic oxime-carbamate and hydrogen bond interactions. Macromol. Rapid Commun. 45, 2400022 (2024). https://doi.org/10.1002/marc.202400022

12. Yang, W. et al. Synthesis of vanillin-based polyurethane with super thermal stability and free-radical-scavenging activity. Macromolecules 58, 526-537 (2025). https://doi.org/10.1021/acs.macromol.4c01354

13. Shi, Z. et al. Waterborne Polyurethane Micelles Reinforce PEO-Based Electrolytes for Lithium Metal Batteries. Small 20, 2407293 (2024). https://doi.org/10.1002/smll.202407293

14. Shi, Z. et al. Elastomeric Electrolytes via Thiourethane Dynamic Chemistry and Hierarchical Hydrogen-Bonding Interactions. Macromolecules 56, 10179-10191 (2023). https://doi.org/10.1021/acs.macromol.3c01695

15. Shi, Z. et al. Deep eutectic solvent-assisted phase separation for polyurea-based polymer electrolytes. Chem. Eng. J. 468, 143687 (2023). https://doi.org/10.1016/j.cej.2023.143687

16. Zhou, B. et al. A flexible, self-healing and highly stretchable polymer electrolyte via quadruple hydrogen bonding for lithium-ion batteries. J. Mater. Chem. A 6, 11725-11733 (2018). https://doi.org/10.1039/c8ta01907j
17. Zhou, B. et al. Self-Healing Polymer Electrolytes Formed via Dual-Networks: A New Strategy for Flexible Lithium Metal Batteries. Chem. Eur. J. 24, 19200-19207 (2018). https://doi.org/10.1002/chem.201803943
18. Li, M. et al. Self-healing and recyclable photonic elastomers based on a water soluble supramolecular polymer. Mater. Chem. Front. 3, 2707-2715 (2019). https://doi.org/10.1039/c9qm00454h
19. Tran, H. et al. Design of functional and sustainable polymers assisted by artificial intelligence. Nat. Rev. Mater. 9, 866-886 (2024). https://doi.org/10.1038/s41578-024-00708-8
20. Tkatchenko, A. Machine learning for chemical discovery. Nat. Commun. 11, 4125 (2020). https://doi.org/10.1038/s41467-020-17844-8
21. Kuenneth, C. & Ramprasad, R. polyBERT: a chemical language model to enable fully machine-driven ultrafast polymer informatics. Nat. Commun. 14, 4099 (2023). https://doi.org/10.1038/s41467-023-39868-6
22. Goodall, R. E. A. & Lee, A. A. Predicting materials properties without crystal structure: deep representation learning from stoichiometry. Nat. Commun. 11, 6280 (2020). https://doi.org/10.1038/s41467-020-19964-7
23. Cheng, Y. et al. Accelerated development of novel biomass-based polyurethane adhesives via machine learning. ACS Appl. Mater. Interfaces 17, 15959-15968 (2025). https://doi.org/10.1021/acsami.4c20371

24. Meng, Y., Lin, Y. & Zhang, A. Prediction and explanation of properties in multicomponent polyurethane elastomers: integrating molecular dynamics and machine learning. Macromolecules 57, 10912-10925 (2024). https://doi.org/10.1021/acs.macromol.4c02559

25. Li, K. et al. Machine learning-guided discovery of ionic polymer electrolytes for lithium metal batteries. Nat. Commun. 14, 2789 (2023). https://doi.org/10.1038/s41467-023-38493-7

26. Wu, H. et al. Machine-learning-assisted design of mechanically robust room-temperature self-healing epoxy resins. Macromolecules 58, 5101-5109 (2025). https://doi.org/10.1021/acs.macromol.5c00667

27. Jablonka, K. M. et al. Bias free multiobjective active learning for materials design and discovery. Nat. Commun. 12, 2312 (2021). https://doi.org/10.1038/s41467-021-22437-0

28. Zhang, Y. et al. Unsupervised discovery of solid-state lithium ion conductors. Nat. Commun. 10, 5260 (2019). https://doi.org/10.1038/s41467-019-13214-1

29. Qu, J. et al. Leveraging language representation for materials exploration and discovery. npj Comput. Mater. 10, 58 (2024). https://doi.org/10.1038/s41524-024-01231-8

30. Baird, S. G., Diep, T. Q. & Sparks, T. D. DiSCoVeR: a materials discovery screening tool for high performance, unique chemical compositions. Digit. Discov. 1, 226-240 (2022). https://doi.org/10.1039/D1DD00028D

31. Zhang, J. et al. Mining solid-state electrolytes from metal-organic framework databases through large language models and representation clustering. J. Am. Chem. Soc. 147, 40496-40506 (2025). https://doi.org/10.1021/jacs.5c12212

32. Zhao, Y., Mulder, R. J., Houshyar, S. & Le, T. C. A review on the application of molecular descriptors and machine learning in polymer design. Polym. Chem. 14, 3325-3346 (2023). https://doi.org/10.1039/D3PY00395G

33. Menon, A., Thompson-Colón, J. A. & Washburn, N. R. Hierarchical machine learning model for mechanical property predictions of polyurethane elastomers from small datasets. Front. Mater. 6, 87 (2019). https://doi.org/10.3389/fmats.2019.00087

34. Weeratunge, H. et al. A machine learning accelerated inverse design of underwater acoustic polyurethane coatings. Struct. Multidiscip. Optim. 65, 213 (2022). https://doi.org/10.1007/s00158-022-03322-w

35. Pugar, J. A. et al. Elucidating the physicochemical basis of the glass transition temperature in linear polyurethane elastomers with machine learning. J. Phys. Chem. B 124, 9722-9733 (2020). https://doi.org/10.1021/acs.jpcb.0c06439

36. Khajeh, A. et al. Early prediction of ion transport properties in solid polymer electrolytes using machine learning and system behavior-based descriptors of molecular dynamics simulations. Macromolecules 56, 4787-4799 (2023). https://doi.org/10.1021/acs.macromol.3c00416

37. Yue, T., He, J. & Li, Y. Polyuniverse: generation of a large-scale polymer library using rule-based polymerization reactions for polymer informatics. Digit. Discov. 3, 2465-2478 (2024). https://doi.org/10.1039/D4DD00196F

38. Hu, Y. et al. Machine-learning-assisted design of highly tough thermosetting polymers. ACS Appl. Mater. Interfaces 14, 55004-55016 (2022). https://doi.org/10.1021/acsami.2c14290

39. Zhou, Y., Wen, J. & Nie, Y. Microscopic mechanisms of self-healing in polymers revealed by molecular simulations and machine learning. Macromolecules 57, 3258-3270 (2024). https://doi.org/10.1021/acs.macromol.4c00338

40. Chen, J. et al. Novel molecular-level insight into the self-healing behavior and mechanism of polyurethane-urea elastomer based on a noncovalent strategy. Macromolecules 55, 4776-4789 (2022). https://doi.org/10.1021/acs.macromol.2c00608

41. McInnes, L., Healy, J., Saul, N. & Grossberger, L. UMAP: Uniform manifold approximation and projection. J. Open Source Softw. 3, 861 (2018). https://doi.org/10.21105/joss.00861

42. McInnes, L., Healy, J. & Astels, S. hdbscan: Hierarchical density based clustering. J. Open Source Softw. 2, 205 (2017). https://doi.org/10.21105/joss.00205

43. He, Y., Xie, D. & Zhang, X. The structure, microphase-separated morphology, and property of polyurethanes and polyureas. J. Mater. Sci. 49, 7339-7352 (2014). https://doi.org/10.1007/s10853-014-8458-y

44. Jia, Y. et al. A fluorine-based strong and healable elastomer with unprecedented puncture resistance for high performance flexible electronics. Sci. Bull. 69, 1875-1886 (2024). https://doi.org/10.1016/j.scib.2024.03.047

45. Jia, Y. et al. Spider Silk-Like Nanodomain Spacings Enable Mechanically Robust and Healable Elastomers with Record-High Puncture Resistance. Small 22, e14193 (2026). https://doi.org/10.1002/smll.202514193

46. Li, Z. et al. Healable and recyclable elastomers with record-high mechanical robustness, unprecedented crack tolerance, and superhigh elastic restorability. Adv. Mater. 33, 2101498 (2021). https://doi.org/10.1002/adma.202101498

47. Guan, T. et al. Mechanically robust skin-like poly(urethane-urea) elastomers cross-linked with hydrogen-bond arrays and their application as high-performance ultrastretchable conductors. Macromolecules 55, 5816-5825 (2022). https://doi.org/10.1021/acs.macromol.2c00492

48. Guo, R. et al. Extremely strong and tough biodegradable poly(urethane) elastomers with unprecedented crack tolerance via hierarchical hydrogen-bonding interactions. Adv. Mater. 35, 2212130 (2023). https://doi.org/10.1002/adma.202212130

49. Xu, F., Li, H. & Li, Y. Sea cucumber-inspired polyurethane demonstrating record-breaking mechanical properties in room-temperature self-healing ionogels. Adv. Mater. 36, 2412317 (2024). https://doi.org/10.1002/adma.202412317

50. Wang, C. et al. Robust self-healing polyurethane-based solid-state ion-conductive elastomers with exceptional strength and ionic conductivity for multifunctional strain sensors and triboelectric nanogenerators. Adv. Mater. 37, 2504361 (2025). https://doi.org/10.1002/adma.202504361

51. Hao, Y., Zhu, G. & Li, B. Self-healing polyurethane-urea elastomers with high strength and toughness based on dynamic hindered urea bonds and hydrogen bonds. Ind. Eng. Chem. Res. 63, 19350-19358 (2024). https://doi.org/10.1021/acs.iecr.4c02340

52. Li, J. et al. Recyclable, self-healing itaconic acid-based polyurethane networks with dynamic boronic ester bonds for recoverable adhesion application. Polymer 256, 125227 (2022). https://doi.org/10.1016/j.polymer.2022.125227

53. Ren, S. et al. Simultaneous robustness, reprocessing and self-healing of castor oil-based polyurethane vitrimers enabled by supramolecular nitrogen-coordinated dynamic covalent boronic ester. Ind. Crops Prod. 206, 117738 (2023). https://doi.org/10.1016/j.indcrop.2023.117738

54. Zhou, H. et al. Reversible and ultrastrong epoxy-polyurethane adhesives with microphase separation. Adv. Funct. Mater. 35, 2506419 (2025). https://doi.org/10.1002/adfm.202506419

55. Lai, Y. et al. Colorless, transparent, robust, and fast scratch-self-healing elastomers via a phase-locked dynamic bonds design. Adv. Mater. 30, 1802556 (2018). https://doi.org/10.1002/adma.201802556

56. Khatib, M., Zohar, O., Saliba, W., Srebnik, S. & Haick, H. Highly efficient and water-insensitive self-healing elastomer for wet and underwater electronics. Adv. Funct. Mater. 30, 1910196 (2020). https://doi.org/10.1002/adfm.201910196

57. Li, W. et al. High-strength self-healing moisture-curable polyurethane enabled by synergistic dynamic disulfide bonds and multiple hydrogen bonds. Polymer 336, 128927 (2025). https://doi.org/10.1016/j.polymer.2025.128927

58. Song, Y., Liu, Y., Qi, T. & Li, G. L. Towards dynamic but supertough healable polymers through biomimetic hierarchical hydrogen-bonding interactions. Angew. Chem. Int. Ed. 57, 13838-13842 (2018). https://doi.org/10.1002/anie.201807622

59. Shi, Z. et al. In Situ Construction of Polymer Electrolytes with Dynamic Covalent Networks via Initiator-Free Thiol-Methacrylate Radical Polymerization. Macromolecules 57, 1229-1237 (2024). https://doi.org/10.1021/acs.macromol.3c01997

60. Jo, Y. H. et al. Self-Healing Solid Polymer Electrolyte Facilitated by a Dynamic Cross-Linked Polymer Matrix for Lithium-Ion Batteries. Macromolecules 53, 1024-1032 (2020). https://doi.org/10.1021/acs.macromol.9b02305

61. Li, S. et al. Covalently cross-linked polymer stabilized electrolytes with self-healing performance via boronic ester bonds. Polym. Chem. 11, 5893-5902 (2020). https://doi.org/10.1039/d0py00728e

62. Zhou, B. et al. Self-Healing and Recyclable Polymer Electrolyte Enabled with Boronic Ester Transesterification for Stabilizing Ion Deposition. Adv. Funct. Mater. 33, 2212005 (2023). https://doi.org/10.1002/adfm.202212005

63. Gangjee, A., Yu, J., McGuire, J. J., Cody, V., Galitsky, N., Kisliuk, R. L. & Queener, S. F. Design, synthesis, and X-ray crystal structure of a potent dual inhibitor of thymidylate synthase and dihydrofolate reductase as an antitumor agent. J. Med. Chem. 43, 3837-3851 (2000). https://doi.org/10.1021/jm000200l

64. Guo, Z. et al. Room-temperature healable, recyclable and mechanically super-strong poly(urea-urethane)s cross-linked with nitrogen-coordinated boroxines. J. Mater. Chem. A 9, 11025-11032 (2021). https://doi.org/10.1039/D1TA00902H

Author contributions

Dian Liu: Conceptualization, data curation, formal analysis, investigation, methodology, visualization, and writing-original draft. Zhen Shi: Conceptualization, Investigation, methodology, validation, visualization, and writing-review and editing. Junchen Meng: Investigation, methodology, validation, visualization. Xiaoyu Ji: Funding acquisition, project administration, and writing-review and editing. Zhigang Xue: Conceptualization, Funding acquisition, project administration, supervision, and writing-review and editing. All authors approved the final version of the manuscript.

Funding

This work was financially supported by the National Natural Science Foundation of China (52403285 and 52573079) and the Innovation and Talent Recruitment Base of New Energy Chemistry and Device (B21003).

Acknowledgements

The authors acknowledge the assistance of the Analysis and Testing Center team at Huazhong University of Science and Technology for their support in material

characterization.

Competing interests

The authors declare no competing financial interests.

Additional information

Supplementary information accompanies this article.

Correspondence and requests for materials should be addressed to Xiaoyu Ji or Zhigang Xue.

Supplementary Files

This is a list of supplementary files associated with this preprint. Click to download.

- SupplementaryTableS2.xlsx
- SupplementaryTableS1.xlsx
- SupplementaryVideo.mp4
- SupplementaryInformation.docx